



OPEN

Grain-boundary segregation of magnesium in doped cuprous oxide and impact on electrical transport properties

João Resende^{1,2}✉, Van-Son Nguyen³, Claudia Fleischmann⁴, Lorenzo Bottiglieri¹, Stéphane Brochen¹, Wilfried Vandervorst^{4,5}, Wilfried Favre³, Carmen Jiménez¹, Jean-Luc Deschanvres¹ & Ngoc Duy Nguyen²

In this study, we report the segregation of magnesium in the grain boundaries of magnesium-doped cuprous oxide (Cu₂O:Mg) thin films as revealed by atom probe tomography and the consequences of the dopant presence on the temperature-dependent Hall effect properties. The incorporation of magnesium as a divalent cation was achieved by aerosol-assisted metal organic chemical vapour deposition, followed by thermal treatments under oxidizing conditions. We observe that, in comparison with intrinsic cuprous oxide, the electronic transport is improved in Cu₂O:Mg with a reduction of resistivity to $13.3 \pm 0.1 \Omega \text{ cm}$, despite the reduction of hole mobility in the doped films, due to higher grain-boundary scattering. The Hall carrier concentration dependence with temperature showed the presence of an acceptor level associated with an ionization energy of $125 \pm 9 \text{ meV}$, similar to the energy value of a large size impurity–vacancy complex. Atom probe tomography shows a magnesium incorporation of 5%, which is substantially present at the grain boundaries of the Cu₂O.

Cuprous oxide (Cu₂O) thin films have attracted attention for photovoltaic and transparent electronic applications due to their tuneable direct bandgap, p-type conductivity, non-toxicity, abundance and low-cost productivity^{1,2}. The p-type behavior of cuprous oxide arises from the special configuration of the valence band, formed by 3d¹⁰ levels of the Cu⁺ cation. The existence of these different levels contribute to a less localized population of holes, which improves the mobility of these charges³. For the generation of holes, the copper vacancies, V_{Cu} , are considered as the most favorable defect from the point of view of formation energy. They are generally created during post-deposition annealing treatments under oxidizing conditions^{4–6}. At temperatures below 300 °C, Cu₂O thin films show a decrease of the resistivity down to values as low as 100 Ω cm, due to an increase of the p-type charge carrier concentration which can reach up to 10¹⁶ cm⁻³^{4,7}. To further increase the concentration of charge carriers, copper oxide can be doped with several elements such as nitrogen^{8–11}, sodium¹², strontium¹³, or magnesium^{14–16}, which also impact their optical performances compared to pure Cu₂O. The use of these dopants seems to reduce the resistivity of Cu₂O thin films, by increasing the density of holes from 10¹⁷ to 10¹⁹ cm⁻³. Additionally, they are responsible for the creation of an extra acceptor level in Cu₂O^{9,13}. In the specific case of magnesium incorporation in Cu₂O, this dopant showed a strong effect on the resistivity, reaching values as low as 7 Ω cm¹⁶, by increasing the charge carrier density up to $8.1 \times 10^{17} \text{ cm}^{-3}$. Besides, this dopant increases the stability of the Cu₂O phase under thermal oxidizing treatments¹⁷. Additionally, several all-oxide solar cells have been produced with Mg-doped Cu₂O, by using TiO₂¹⁴ and ZnO¹⁵ as n-type counterparts, reporting efficiency values close to 1%. Nevertheless, there lacks a detailed understanding of the dopant location in the structure of Cu₂O and of the underlying mechanism at the origin of the increase of the carrier density.

In this study, we analyse the spatial distribution of magnesium as dopant in polycrystalline copper oxide by atom probe tomography and its direct impact on the electrical transport properties by temperature-dependent Hall effect. Additionally, intrinsic and magnesium-doped Cu₂O (Cu₂O:Mg) thin films have been thermally annealed in air at temperatures above 250 °C to further investigate the generation of charge carriers in the thin films.

¹Univ. Grenoble Alpes, CNRS, Grenoble INP, LMGP, 38000 Grenoble, France. ²Département de Physique, CESAM/Q-MAT, SPIN, Université de Liège, 4000 Liège, Belgium. ³CEA, INES, LITEN, 50 Avenue du lac Léman, 73375 Le Bourget-du-lac, France. ⁴IMEC, Kapeldreef 75, 3001 Heverlee, Belgium. ⁵Instituut Voor Kern- en Stralingsfysica, KU Leuven, Celestijnenlaan 200D, 3001 Leuven, Belgium. ✉email: ngocduy.nguyen@uliege.be

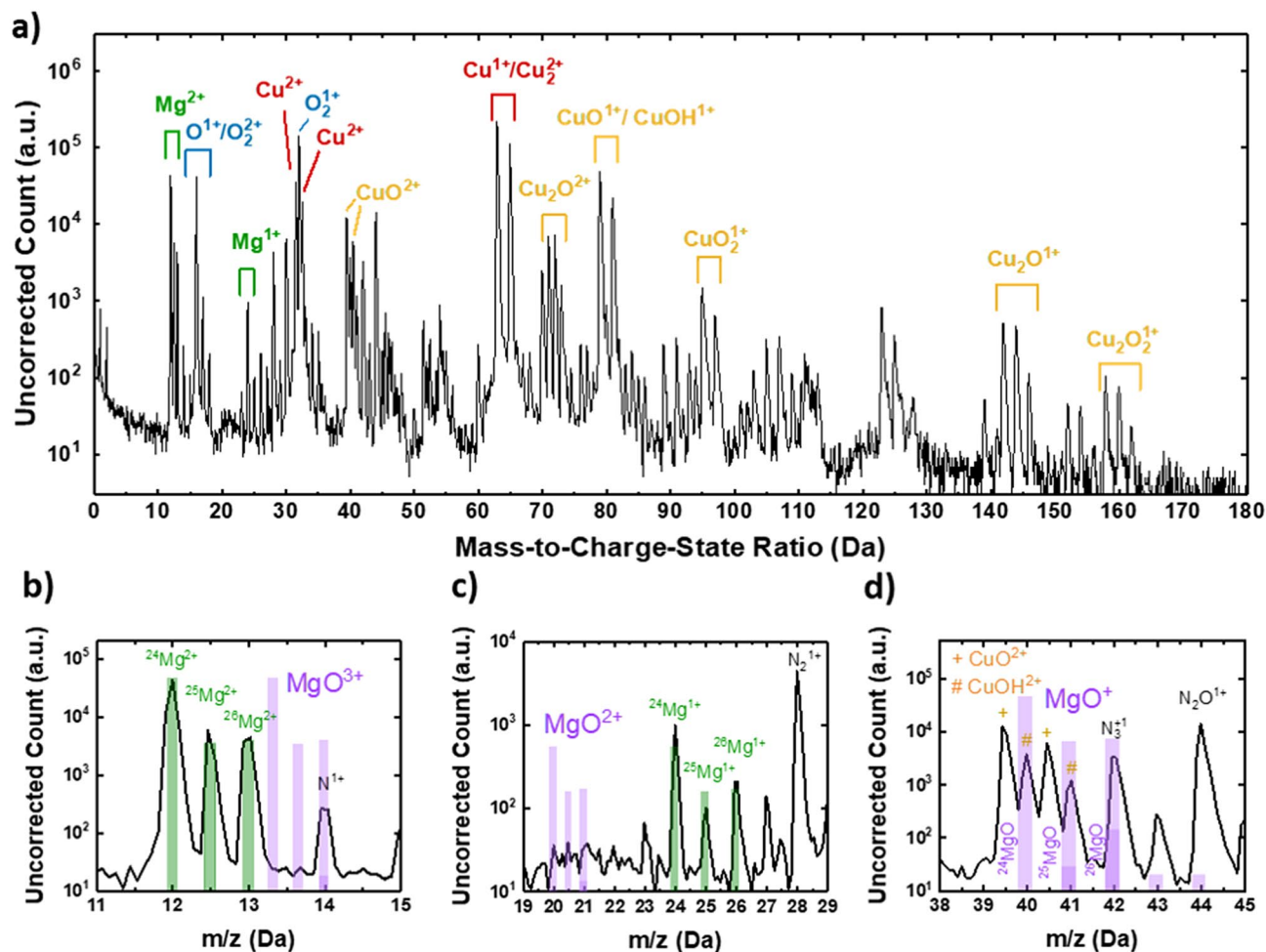


Figure 1. Atom probe mass spectra averaged over the volume corresponding to the as-deposited $\text{Cu}_2\text{O}:\text{Mg}$ film. The ions collected from the Si substrate are not shown for clarity: (a) full mass spectrum with the relevant atomic and molecular ion species highlighted; (b–d) show selected regions of the spectrum shown in (a), in which the location and abundance of the peaks originating from Mg^{nx} ions and MgO_x^{nx} ions shown by green and purple bars, respectively.

Results

The as-deposited Cu_2O and $\text{Cu}_2\text{O}:\text{Mg}$ thin films were routinely characterized in order to measure the thickness by scanning electron microscope (SEM) cross section imaging and the resistivity by the Van der Pauw method. The intrinsic Cu_2O thin films presented a thickness of 240 ± 10 nm with a resistivity of 93 ± 1 Ω cm, while the $\text{Cu}_2\text{O}:\text{Mg}$ films were 180 ± 10 nm thick, with a resistivity of 61.3 ± 0.4 Ω cm.

Magnesium location in copper oxide thin films. Atom probe tomography (APT) is ideally suited to study the 3-dimensional dopant distribution^{18–23}. The basic principle of APT, including the procedure for building the tomographic reconstruction, is described in detail elsewhere^{24–26}. APT analysis of the as-deposited $\text{Cu}_2\text{O}:\text{Mg}$ film yielded an average Mg incorporation of 5%, computed with respect to both cations ($\text{Mg}/(\text{Mg} + \text{Cu})$). Both singly Mg^+ and doubly charged Mg^{2+} ions are observed in the APT mass spectrum (Fig. 1a), with a higher intensity of the doubly charged ions. No traces of magnesium oxides were found in the mass spectrum, as depicted in Fig. 1b–d by purple bars, which represent the location and expected peak ratio based on the natural isotopic abundance of the MgO^+ , MgO^{2+} and MgO^{3+} ions. The peaks at 40 and 41 Da (Fig. 1d, represented by #) were assigned to CuOH^{2+} due to their matching ratio with the isotopic abundance of the Cu hydride rather than the MgO^+ ion^{25,26}. No carbon contamination from the AA-MOCVD process was detected in the APT mass spectrum. The peaks at 12 Da ($=\text{C}^+$ or Mg^{2+}), 12.5 Da and 13 Da show a very good agreement with the expected isotopic ratio of Mg^{2+} , ruling out a contribution of C^+ ions to the peak at 12 Da.

The mass spectrum further contains various singly ($n=1$) and doubly ($n=2$) charged Cu molecular ions such as CuO^n , Cu_2O^{n+} , CuO_2^{n+} , $\text{Cu}_2\text{O}_2^{n+}$ and CuOH^n . Charged molecules, including hydride ions, are commonly detected when field-evaporating covalently or ionically bonded materials^{27,28}, and hence their presence in the mass spectrum does not reflect the chemistry of the Cu_2O film. Indeed, previous studies on $\text{Cu}_2\text{O}:\text{Mg}$ thin films confirm the sole presence of crystalline cuprous oxide, Cu_2O , by XRD, Raman, TEM and FTIR^{14,16,17}. Considering

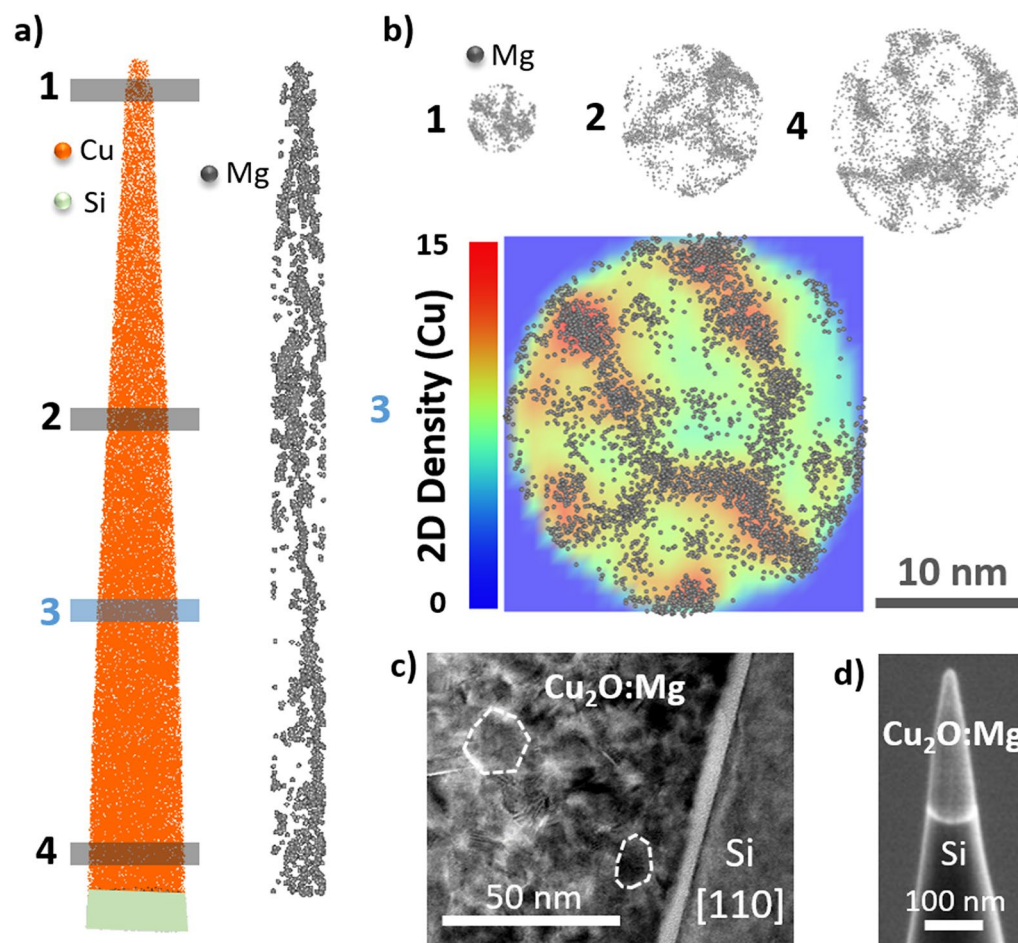


Figure 2. 3D atomic map of the as-deposited $\text{Cu}_2\text{O}:\text{Mg}$ film for which the tip shape shown in (d) was used to guide the tomographic reconstruction. (a) 3D atomic map of Cu and Si atoms is presented by orange and light green dots, respectively (left-hand side) and distribution of Mg in a 1 nm thick slice parallel to the APT specimen axis is shown, presenting a cross-sectional view of the film in dark grey dots (right-hand side). (b) 10 nm thick slices taken at different positions from top to bottom (number 1–4) represent a planar view of the film. In 1, 2 and 4 the 2D Mg ion maps are shown and in 3 this is superimposed with the Cu ion 2D density color map. (c) TEM micrograph of $\text{Cu}_2\text{O}:\text{Mg}$ thin film cross-section deposited on silicon and (d) SEM micrograph of the $\text{Cu}_2\text{O}:\text{Mg}$ specimen before APT analysis.

the complex processes that are intrinsically related to field evaporation and/or the behaviour of molecular ions in high electric fields (e.g. field-induced dissociation²⁷), it is typically very cumbersome to draw reliable and quantitative information on the charge state of the analysed material based on APT mass spectra. Other unidentified peaks in Fig. 1a correspond to combinations of complex ions, as no match was possible to be established.

The spatial distribution of the Mg atoms is inhomogeneous throughout the Cu_2O film, visible in Fig. 2a, with a local enrichment that resembles the grain boundary (GB) network of the film, with a grain size between 10 and 20 nm, as presented in Fig. 2c of TEM imaging. The grains present a round-like shape, with some straight edges, contrarily to the common columnar growth of intrinsic Cu_2O oriented perpendicular to the substrate prepared by MOCVD²⁹.

Representative 2-dimensional (2D) Mg ion maps are shown in both cross-section and planar views of the film in Fig. 2a,b, respectively, as well as the tip SEM image before APT analysis, visible in Fig. 2d. The planar Mg distribution correlates well with regions of higher atomic density in the 2D Cu ion density map, Fig. 2b slice 3, suggesting an Mg segregation into grain boundaries. Atomic density variations in the 3D volume reconstruction (or on the detector) can be ascribed to ion trajectory aberrations (deflection of the ions) and associated local magnification effects^{20,25,30–32}. These typically originate from local disturbances in the electric field distribution, which often result from dissimilarities in the local curvature of the APT tip developed around microstructural features such as grain boundaries, interfaces, precipitates etc.

The local presence of Mg in the edges of the grains can be observed in Fig. 2b slice 3 and 4, where the dopant shows the shape of vertical grain boundaries to the axis of analysis. Nevertheless, in both slices 1 and 2 of Fig. 2b, we can observe a higher concentration of magnesium, similar to horizontal grain boundaries to the analysis axis, attributed to be edges of several grains. Therefore, the four presented slices provide us the evidence of magnesium

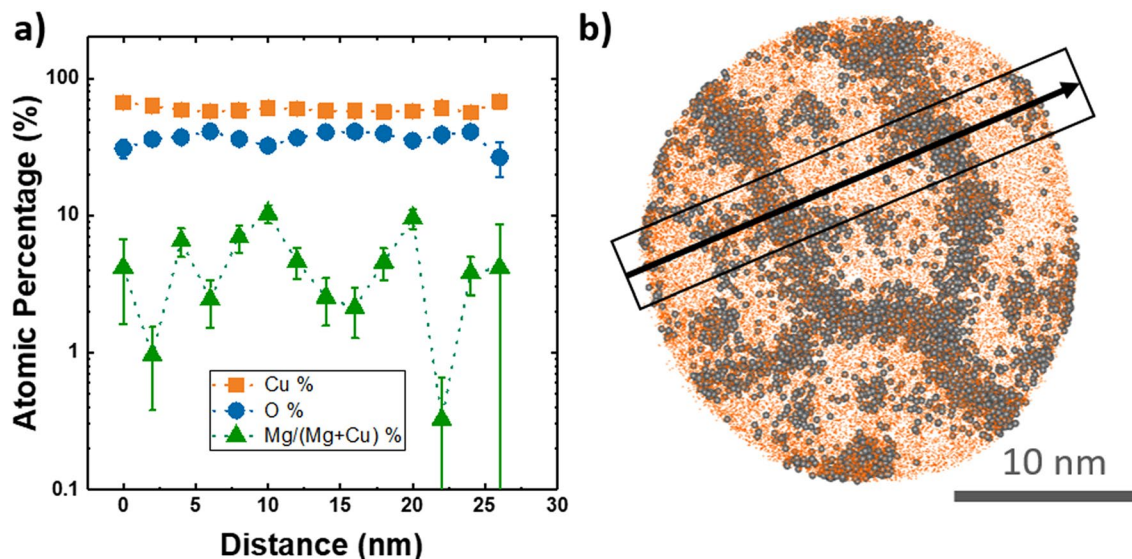


Figure 3. (a) Local atomic concentration profiles (Cu, O and Mg/(Mg + Cu) ratio) and (b) 2D ion map with Cu in orange and Mg in gray, extracted from a 10 nm thick slice across the APT specimen (plane-view of as-deposited $\text{Cu}_2\text{O}:\text{Mg}$ film) close to the position 4 indicated in Fig. 2a). The box and thick arrow indicate the location and direction of the profile shown in (a).

presence at both horizontal and vertical grain boundaries to the analysis axis. Additionally, the APT results provided a complementary information to High-Angle Annular Dark-Field (HAADF) images combined with Energy-dispersive X-ray spectroscopy (EDS) elemental mapping, as the location of Mg atoms was unachieved, presented in Supplementary Material Figure S1.

The quantitative analysis of the Mg distribution is hampered by the small grain size, between 10 and 20 nm, and the random orientation of the grain boundaries within the film. Hence a clear separation between the grain and a grain boundary cannot always be made in the reconstructed data. A one-dimensional concentration profile computed across the grain boundaries, identified based on the Mg^{1+} and Mg^{2+} ion distribution, Fig. 3a, reveals that the Mg/(Mg + Cu) concentration drops from ~7 at% to below 1 at% from the grain boundary to the bulk of the grain. A 2D ion map of Cu and Mg from a 10 nm thick slice of the APT tip is visible in Fig. 3b. However, it remains inconclusive whether the grain is fully depleted of Mg. Yet, the APT data clearly reveal the segregation of Mg atoms to the grain boundaries in the Cu_2O film, even though the conclusion remains more qualitative at this moment. The local fluctuations in the oxygen concentration profile (Fig. 3a) should not be over interpreted, as these could originate from local electric field variations along this direction, i.e., at the grain boundaries the field is lower than in the surrounding areas. A field-dependent quantification accuracy for oxygen-containing compounds has been reported before, in which the oxygen fraction was underestimated at low field³³.

Temperature-dependent Hall effect measurements. The impact of the 5% Mg incorporated in the copper oxide films combined with oxidizing thermal treatments on the electrical properties was assessed via monitoring of the resistivity during different annealing steps (250, 350 and 450 °C) as well as corresponding temperature-dependent Hall effect measurements. For intrinsic Cu_2O samples we obtained a reduction of the resistivity only during the 250 °C annealing step, leading to a final room temperature value for the resistivity of $80 \pm 1 \Omega \text{ cm}$, presented in Table 1. The annealing treatments at 350 °C and 450 °C increase the resistivity, leading to a final resistance higher than that of the original film, especially in the 450 °C case, where the resistivity reaches $1650 \pm 10 \Omega \text{ cm}$, allegedly attributed to the formation of CuO, as previously reported¹⁷. For the $\text{Cu}_2\text{O}:\text{Mg}$ thin films, we observed a different trend when compared to the intrinsic Cu_2O samples, since all the thermal treatments lead to a reduction of the final resistivity at room temperature compared to the initial value, with the lowest resistivity value of $13.3 \pm 0.1 \Omega \text{ cm}$ observed for the sample annealed at 450 °C, presented on Table 1. A more detailed discussion of the resistivity variation during each annealing treatment is included in the Supplementary Material, Figure S2.

The electrical nature of the defects formed during the thermal treatments was then evaluated by temperature-dependent Hall effect measurements from 220 to 400 K. The results thereby confirmed that all samples indeed showed p-type conductivity. Table 1 shows the effect of the annealing temperature on mobility and charge-carrier density of the intrinsic and Mg-doped Cu_2O films. For the intrinsic Cu_2O case, the as-deposited sample and the samples annealed below 450 °C show a mobility maintained roughly constant at about $7\text{--}9 \text{ cm}^2 \text{ V}^{-1} \text{ s}^{-1}$, consistent with a grain-boundary-limited type of conduction in randomly oriented Cu_2O grains^{34–36}. The sample annealed at 450 °C, reached a resistivity above $1000 \Omega \text{ cm}$, exceeding the experimental range of the setup, as CuO is formed in particularly at the grain boundaries, which leads to a decrease of mobility, as previously reported²⁹. The free charge carrier density, associated to holes, varied in the Cu_2O samples showing a maximum Hall carrier density of $9.2 \times 10^{15} \text{ cm}^{-3}$ for the sample annealed at 250 °C. In the case of the $\text{Cu}_2\text{O}:\text{Mg}$ films, the carrier mobility ranges between 2 and $3 \text{ cm}^2 \text{ V}^{-1} \text{ s}^{-1}$, i.e. lower than for intrinsic sample, while the charge carrier

Thin films	Anneal. temp. (°C)	ρ (Ω cm)	μ ($\text{cm}^2 \text{V}^{-1} \text{s}^{-1}$)	p (cm^{-3})	E_{A1} (meV)	N_{A1} (cm^{-3})	E_{A2} (meV)	N_{A2} (cm^{-3})	$N_A - N_D$ (cm^{-3})
Cu_2O	–	93 ± 1	9.7 ± 0.1	$6.1 \times 10^{15} \pm 0.1 \times 10^{15}$	258	7.0×10^{17}	–	–	6.0×10^{17}
	250	80 ± 1	8.4 ± 0.6	$9.2 \times 10^{15} \pm 0.6 \times 10^{15}$	249	9.5×10^{17}	–	–	8.5×10^{17}
	350	155 ± 2	7.3 ± 0.4	$5.6 \times 10^{15} \pm 0.2 \times 10^{15}$	247	5.9×10^{17}	–	–	4.9×10^{17}
	450	1650 ± 10	–	–	–	–	–	–	–
$\text{Cu}_2\text{O:Mg}$	–	61.3 ± 0.4	2.4 ± 0.1	$4.3 \times 10^{16} \pm 0.2 \times 10^{16}$	251	4.0×10^{18}	124	4.7×10^{16}	4.0×10^{18}
	250	24.4 ± 0.2	2.8 ± 0.2	$9.3 \times 10^{16} \pm 0.5 \times 10^{16}$	251	7.7×10^{18}	113	1.2×10^{17}	7.7×10^{18}
	350	27.7 ± 0.1	2.7 ± 0.5	$8.8 \times 10^{16} \pm 0.5 \times 10^{16}$	251	6.3×10^{18}	126	1.4×10^{17}	6.3×10^{18}
	450	13.3 ± 0.1	2.3 ± 1	$2.9 \times 10^{17} \pm 1.8 \times 10^{17}$	251	9.5×10^{19}	136	2.2×10^{17}	9.5×10^{19}

Table 1. Electrical transport properties of Cu_2O and $\text{Cu}_2\text{O:Mg}$ (5%) films, as-deposited and thermally annealed in air at 250 °C, 350 °C and 450 °C. Resistivity, mobility and charge carrier density values were determined at room temperature by Hall effect measurements. Ionization energies and concentrations of the two acceptor levels, as well as the difference between acceptor and donor concentrations are obtained from the fitting of temperature-dependent Hall carrier density.

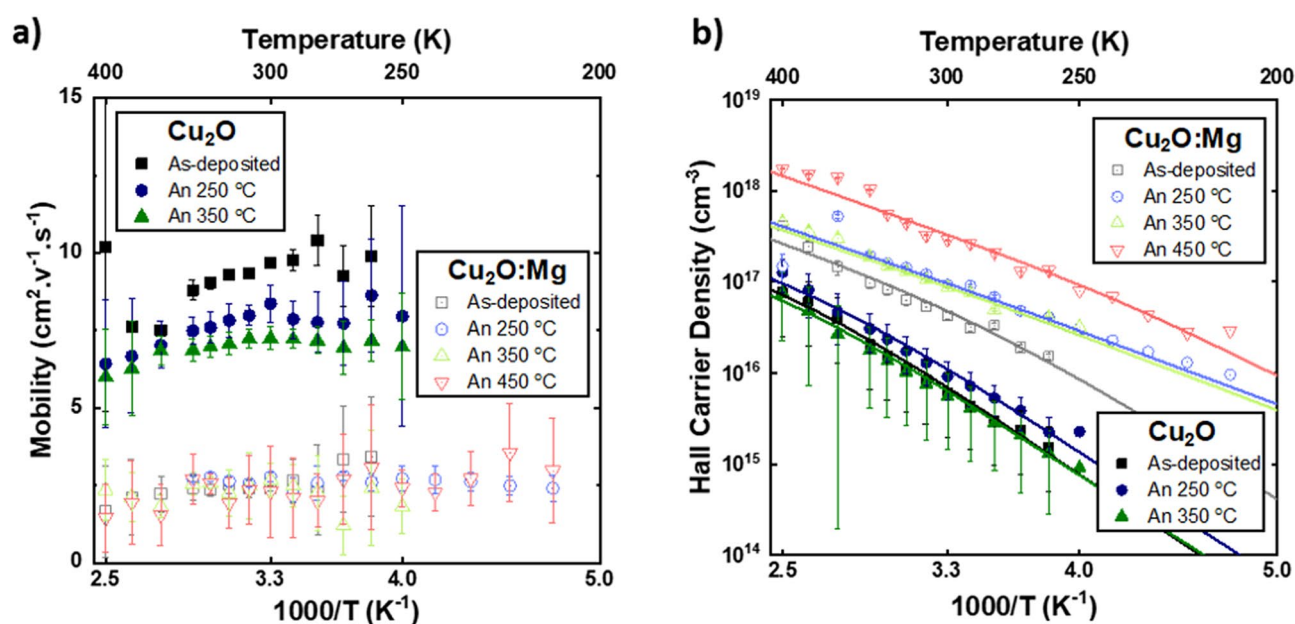


Figure 4. Temperature-dependent Hall effect measurements of Cu_2O and $\text{Cu}_2\text{O:Mg}$ thin films. (a) Mobility (μ) and (b) Hall carrier density (p) as a function of the reciprocal temperature, where the lines correspond to the charge balance equation fit.

density increases after thermal annealing treatments, presenting a maximum for the film annealed at 450 °C, with a value of $2.9 \times 10^{17} \text{ cm}^{-3}$.

Figure 4 shows the temperature dependence of the mobility and carrier density obtained from Hall effect measurements in the range 220–400 K for the two groups of films, Cu_2O and $\text{Cu}_2\text{O:Mg}$. The data obtained for the resistivity are given in Supplementary Material, Figure S3. The curves of the carrier mobility in intrinsic films show small variations in the temperature range of the experiment, while constant values are obtained for the $\text{Cu}_2\text{O:Mg}$ films. The Cu_2O film in the as-deposited state has the highest carrier mobility values, reducing with increasing annealing temperature. No clear trend is observed for the doped films. The Hall carrier density is reduced with temperature decrease, as expected for an oxide semiconductor, with the undoped Cu_2O group presenting lower values.

The curves obtained for the temperature-dependent Hall carrier densities for the Cu_2O and $\text{Cu}_2\text{O:Mg}$ thin films (Fig. 4b) have been fitted using a two acceptor levels model. Similar to previous studies³⁷, the numerical solution $p(T)$ of the charge balance equation (CBE) allows us to obtain the influence of temperature on the Cu_2O carrier concentration, while having in consideration Cu_2O as a nondegenerate p-type semiconductor:

$$p(T) + N_D = \frac{N_{A1}}{1 + p(T) \cdot \frac{g_{A1}}{N_V(T)} e^{\frac{E_{A1}}{k_b T}}} + \frac{N_{A2}}{1 + p(T) \cdot \frac{g_{A2}}{N_V(T)} e^{\frac{E_{A2}}{k_b T}}}$$

$$N_V(T) = 2(2\pi m_h^* k_B T)^{3/2} / h^3$$

where N_{A1} , N_{A2} and N_D are atomic densities for, respectively, the first and second acceptor, and the donor, E_{A1} and E_{A2} are the acceptor ionization energies and N_V is the effective density of states in the valence band. The hole effective mass m_h^* was fixed as $0.58 m_0$ as proposed by Hodby et al.³⁸, h and k_B are Planck's and Boltzmann's constants, respectively. As the degeneracy factors are the ratios between the occupied-state and unoccupied-state degeneracies and as the negative spin – orbit splitting suggests to use an unoccupied-state degeneracy of 2 and an occupied state degeneracy of 1, we used the same degeneracy factor for g_{A1} and g_{A2} of 1/2, as proposed by Brochen et al.¹³. In order to allow a simplified fitting procedure using the CBE, the donor density (N_D) was fixed at $3 \times 10^{17} \text{ cm}^{-3}$ in all the different sets of samples. The values of the different acceptor levels concentrations, ionization energies and the difference between acceptors and donor density for each Cu_2O and $\text{Cu}_2\text{O}:\text{Mg}$ case are given in Table 1.

In the case of the intrinsic Cu_2O for the films in the as-deposited state and annealed at 250 °C and 350 °C, only one deep acceptor level is found with an acceptor ionization energy (E_{A1}) of $251 \pm 7 \text{ meV}$, which is generally attributed to the energy of simple copper vacancies, V'_{Cu} , in theoretical³⁹ and experimental⁴⁰ studies. Concerning the concentration of this acceptor state (N_{A1}), the highest value of $9.50 \times 10^{17} \text{ cm}^{-3}$ was found for the sample annealed at 250 °C, which presents the lowest resistivity value of the intrinsic Cu_2O samples.

In the Mg-doped cases, the introduction of a second acceptor level led to an improvement of the model. In order to reduce the number of fitting parameters, it was decided to maintain the ionization energy of the first acceptor level constant, fixed at 251 meV, corresponding to the average value obtained for the undoped Cu_2O samples. Regarding this first acceptor level, its concentration (N_{A1}) increases up to $9.5 \times 10^{19} \text{ cm}^{-3}$ for the $\text{Cu}_2\text{O}:\text{Mg}$ 450 °C annealed sample. This is attributed to an increase of copper simple vacancies (V'_{Cu}) which is the main mechanism for the reduction of resistivity^{41,42} induced by the presence of the magnesium. For the second acceptor level (E_{A2}), we found an ionization energy of $125 \pm 9 \text{ meV}$ with an increasing acceptor concentration (N_{A2}) with the annealing temperature, reaching $2.2 \times 10^{17} \text{ cm}^{-3}$ for the 450 °C annealing temperature.

Discussion

The incorporation of magnesium in copper oxide leads to changes on the grain growth of the thin films. The grains, with a size between 10 and 20 nm, are characterized by a round-like shape, contrarily to the columnar growth previously reported^{29,43}. The APT measurements confirm the presence of the magnesium atoms with a concentration of 5 at% throughout the whole film. However, the dopant is mostly localized at the grain boundaries of the copper oxide polycrystalline film, with the concentration of 7 at% at this region.

The segregation of the magnesium ion has direct impacts on the electronic transport in the oxide semiconductor. We observe a reduction of Hall carrier mobility, which can be attributed to an increase of hole scattering, related to the magnesium incorporation. Copper oxide usually presents a grain-boundary-limited type of conduction³⁴ that governs the electronic transport in the material. Due to the presence of the dopant at the grain boundaries and its effect on the grain growth, we assume that an increase of hole scattering appears at the boundaries of $\text{Cu}_2\text{O}:\text{Mg}$ grains. Therefore, we assume that the presence of magnesium will directly influence the grain-boundary mobility, causing the reduction to the $2.3\text{--}2.8 \text{ cm}^2 \cdot \text{V}^{-1} \cdot \text{s}^{-1}$ range in the $\text{Cu}_2\text{O}:\text{Mg}$ thin films. Additionally, the presence of magnesium inside the grain could also reduce the bulk mobility. Nevertheless, this contribution will not affect the total mobility, as it is a less significant mobility term. Moreover, the temperature-dependent mobility values are roughly constant with the increase of temperature in both sets of samples, which is consistent with a grain-boundary-limited type of conduction in randomly-oriented Cu_2O grains.

In our modelling approach, we considered the thin film conductivity, mobility and carrier density without looking at the spatial distribution of the Mg dopants, since the Hall effect technique is applied on the whole sample and thus sensitive to both bulk and grain boundaries. In general, assuming Matthiessen's rule, the mobility is affected by several scattering mechanisms and the smaller one is responsible for the limitation of the overall mobility value. In the case of $\text{Cu}_2\text{O}:\text{Mg}$ film, it is difficult to observe any clear temperature dependence for the mobility, and its value is well reduced compared to undoped Cu_2O films. For these layers, considering that the Mg distributions obtained from APT technique show higher Mg density in the grain boundaries, one could expect a higher value for the trap density at the grain boundary compared to undoped Cu_2O films, which could affect carrier mobility. In Nguyen et al.⁴⁴, we can find a clear correlation between trap density at the grain boundaries and free carrier density in highly-doped polycrystalline conductive oxides. We find higher carrier concentrations for $\text{Cu}_2\text{O}:\text{Mg}$ films compared to undoped Cu_2O films, which could be related to trap density increase at grain boundaries. Our approach does not consider GB-limited scattering effects, thus we cannot exclude that the second impurity level could be related to the Mg effective doping inside grains and/or a possible influence of the high Mg density at grain boundaries, as observed by APT.

Although the magnesium concentration inside the grain is below 1%, its mere presence induces the formation of a shallower acceptor value with an ionization energy of 125 mV, comparable to the secondary defect observed in $\text{Cu}_2\text{O}:\text{Sr}$ ¹³. This type of defect is attributed to a large size impurity–vacancy complex found previously in Sr-doped Cu_2O , as this defect is a clustering of a two-simple vacancy with the dopant in a tetrahedral position, $[Mg_i - 2V'_{\text{Cu}}]^-$, previously proposed by Isseroff and Carter⁴². A representation of the suggested $[Mg_i - 2V'_{\text{Cu}}]^-$ complex is shown in the Supplementary Material Figure S4. It is expected that this complex prevents the formation of split vacancies for a single cation vacancy, since the divalent cation would assume a position similar to a split copper vacancy (V_{split}) in the crystallographic structure⁴². As a consequence, $\text{Cu}_2\text{O}:\text{Mg}$ materials present an increased response in photoconductivity¹⁴ and exhibit improved chemical stability at high temperatures^{14,17}, as already reported in the literature. Additionally, this complex would further increase the charge carrier density

Dopant	Amount of dopant (%)	Resistivity (Ω cm)	Carrier concentration (cm^{-3})	Acceptor level (eV)	References
Pure Cu_2O	0	150	1.5×10^{15}	210	47
N^-	<0.1	15.2	7×10^{16}	121–140	9,11
F^-	0.9	11.6	1.9×10^{16}	–	48
Cl^-	–	200	8.6×10^{13}	330	49
Na^+	–	0.5	2×10^{19}	22–46	12,46
Zn^{2+}	8.2	100	7×10^{16}	470	50
Ni^{2+}	2	100	2×10^{15}	220–230	51
Sr^{2+}	5	1.2	2.8×10^{17}	104–149	13
Nd^{3+}	5	85	21.5×10^{15}	–	52
Si^{4+}	0.58	12	1×10^{17}	190	45
Mg^{2+}	5	13.3	2.9×10^{17}	113–136	This work

Table 2. Electrical properties of dopants used in Cu_2O thin films: resistivity, carrier concentration at room temperature and acceptor level energy.

after annealing treatments in oxidizing conditions, by a simple copper vacancy doping mechanism assisted by the magnesium incorporation¹³.

The incorporation of different dopants in copper oxide has various types of effects on the electronic transport in the material.

In Table 2, we compare the resistivity, mobility and acceptor level energy values of several Cu_2O doping systems reported in literature. When the resistivity values are reduced by the presence of the dopant, an extra acceptor level with a reduced value or range of activation energy is observed, when compared to the energy level corresponding to copper simple vacancies (V_{Cu}), around 210 meV. The V_{Cu} defects are known to increase the number of free charge carriers and, consequently, they act as dopant species by reducing the resistivity. Furthermore, the generation of free charge carriers is also impacted by the acceptor complex associated with the extrinsic atom. For instance, doping with nitrogen reduces the resistivity down to 1.1 Ω cm, and increases the hole density up to 10^{17} cm^{-3} , by creating an extra acceptor level in Cu_2O at 140 meV⁹. In silicon-doped and strontium-doped films, the charge carriers' density can be further increased to 10^{17} cm^{-3} , which reduces the resistivity to the 1–10 Ω cm range. In these cases an energy value of a large size impurity–vacancy complex was found at 133 and 190 meV, for strontium¹³ and silicon⁴⁵, respectively. In a simple, more straightforward analysis, the presence of dopants such as Mg, Sr or Si in Cu_2O structures would induce a donor-type doping, due to their cation behaviour. Therefore, the resulting p-type conductivity of such extrinsically-doped Cu_2O films is attributed to a charge compensation mechanism, based on the production of simple copper vacancies that leads to an increase of charge carriers, as suggested by Isseroff and Carter⁴² and Minami et al.^{12,46}.

In conclusion, magnesium-doped copper oxide thin films present improved electrical properties when compared to intrinsic thin film, especially after thermal treatments. The dopant is found mostly at the grain boundary of the Cu_2O , as confirmed by Atom Probe Tomography, which reaches 5% in atomic percentage. The magnesium segregation hinders the mobility of these films, reducing it to 2–3 $\text{cm}^2/\text{V s}$. However, the small quantity, below 1%, that is present inside the grain is responsible for the drastic increase of the charge carrier density up to $2.9 \times 10^{17} \text{ cm}^{-3}$, for the film annealed at 450 °C. Temperature-dependent Hall effect measurements led to the determination of a first acceptor level in the range of 247–258 meV attributed to the copper simple vacancy. An additional acceptor level with an activation energy around 113–136 meV was found for the magnesium-doped samples. The use of annealing treatments coupled with the Mg presence in Cu_2O thin films provides new insights into the dopant influence for the copper vacancy generation mechanism.

Methods

Films deposition. A butanol-based solution containing the precursors was used for the deposition by Aerosol-Assisted Metal Organic Chemical Vapour Deposition (AA-MOCVD). The total concentration of the solution was fixed at 30 mM in all cases. The first solution was composed of pure copper acetylacetonate, $\text{Cu}(\text{acac})_2$ [Sigma Aldrich], while in the second one magnesium acetylacetonate, $\text{Mg}(\text{acac})_2$ [Sigma Aldrich] was added to the solution. The $\text{Mg}/(\text{Mg} + \text{Cu})$ ratio in the later solution was fixed at 33 at%, as this level was known to produce sufficiently low resistivity materials in our previous study¹⁶. Ethylenediamine [$\text{C}_2\text{H}_8\text{N}_2$, Sigma Aldrich] with a concentration of 40 mM was added to increase the chemical precursor solubility. The temperature of the substrates, Corning glass 1737 and p-type Si(100), was fixed at 350 °C. The deposition time was 3 h and the solution consumption rate was 1.5 ml min^{-1} with an argon flow of 6 l min^{-1} and oxygen flow of 2.5 l min^{-1} , resulting in an O_2 presence of 29%.

The thermal annealing treatments were performed on a hot-plate exposed to air, coupled with an *in-situ* resistance measurement setup based on a 2-probe system including a KEITHLEY 2400 source-meter. Electrodes on both sides of the samples were made with silver paste. Three stages of temperature (T_a) were chosen, 250 °C, 350 °C and 450 °C, all for 30 min, while the heating and cooling rate was kept constant at 10°C/min.

Characterization techniques. Scanning Electron Microscopy (SEM) and Energy-dispersive X-ray spectroscopy (EDS) were conducted in a FEI Quanta 250 FE-ESEM tool, with an energy beam of 5000 eV. Images of

the film cross section were used to measure the film thickness. Transmission electron microscopy (TEM) imaging was obtained with a JEOL JEM 2010 microscope operating at 200 kV (0.19 nm resolution), provided with an EDS system, INCA Energy TEM 100 X-Max 65 T. Cross-sectional samples were prepared in Cu₂O:Mg film on silicon by tripod polishing resulting in a sample thickness of about 10 µm, glued to a copper grid. Argon ion beam milling was used until perforation of the interface.

Atom probe specimens were prepared using the standard focused ion beam (FIB) lift-out technique (e.g. Thompson et al.⁵³ and Miller et al.⁵⁴) in a dual-beam FIB-SEM setup operating with a Ga⁺ ion source (G3CX from Thermofisher). Laser-assisted atom probe analysis was performed in a reflectron-fitted LEAP 5000XR, equipped with an UV laser (355 nm). The specimen, the as-deposited Cu₂O:Mg film, was analysed at 50 K base temperature, with 25 pJ laser pulses applied at a repetition rate of 125 kHz. In total ~2.400.000 ions were collected, which corresponds to the full Cu₂O film. The analysis was stopped manually in the Si substrate, a few nm after the Cu₂O/Si interface. 3D data reconstruction was performed in IVAS 3.8 using the tip profile evolution taken from an SEM image before APT analysis (Fig. 2d). The image compression factor (ICF), the field factor (k) and the evaporation field (F) were set to 1, 3.3 and 30 V/nm (Cu) so as to achieve a flat Si iso-concentration (1 at%) surface at the Cu₂O/Si interface and a Cu₂O film thickness of around 200 nm, as was measured by SEM from the initial APT specimen. Further details about the APT technique are included in Supplementary Material.

The temperature-dependent transport properties were obtained using a Van der Pauw configuration in a HMS5500 Hall effect measurement setup from Ecopia Microworld. Circular Ag ohmic contacts of 500 µm diameter were deposited at the four corners of 5 × 5 mm² size samples deposited on Corning Glass by electron beam evaporation. The electrical properties were carried out in the temperature range of 80–350 K using liquid Nitrogen cooling, with a permanent magnetic field of 0.57 T. Mobility and carrier concentration values as well as the corresponding error bars were calculated from the average and standard deviation of five different measurements per temperature.

Received: 19 June 2020; Accepted: 16 March 2021

Published online: 08 April 2021

References

- Nandy, S., Banerjee, A., Fortunato, E. & Martins, R. A review on Cu₂O and Cu-based p-type semiconducting transparent oxide materials: Promising candidates for new generation oxide based electronics. *Rev. Adv. Sci. Eng.* **2**, 273–304 (2013).
- Minami, T., Nishi, Y. & Miyata, T. Cu₂O-based solar cells using oxide semiconductors. *J. Semicond.* **37**, (2016).
- Matsuzaki, K. *et al.* Epitaxial growth of high mobility Cu₂O thin films and application to p-channel thin film transistor. *Appl. Phys. Lett.* **93**, 202107 (2008).
- Figueiredo, V. *et al.* Effect of post-annealing on the properties of copper oxide thin films obtained from the oxidation of evaporated metallic copper. *Appl. Surf. Sci.* **254**, 3949–3954 (2008).
- Wang, Y. *et al.* Transmittance enhancement and optical band gap widening of Cu₂O thin films after air annealing. *J. Appl. Phys.* **115**, 2–7 (2014).
- Johan, M. R., Suan, M. S. M., Hawari, N. L. & Ching, H. A. Annealing effects on the properties of copper oxide thin films prepared by chemical deposition. *Int. J. Electrochem. Sci.* **6**, 6094–6104 (2011).
- Eisermann, S. *et al.* Copper oxide thin films by chemical vapor deposition: Synthesis, characterization and electrical properties. *Phys. Status Solidi* **209**, 531–536 (2012).
- Lee, Y. S. *et al.* Nitrogen-doped cuprous oxide as a p-type hole-transporting layer in thin-film solar cells. *J. Mater. Chem. A* **1**, 15416 (2013).
- Ishizuka, S., Kato, S., Maruyama, T. & Akimoto, K. Nitrogen doping into Cu₂O thin films deposited by reactive radio-frequency magnetron sputtering. *Japanese J. Appl. Physics, Part 1 Regul. Pap. Short Notes Rev. Pap.* **40**, 2765–2768 (2001).
- Nordseth, Ø. *et al.* Nitrogen-doped Cu₂O thin films for photovoltaic applications. 1–9 (2019).
- Li, J. *et al.* Probing defects in nitrogen-doped Cu₂O. *Sci. Rep.* **4**, 7240 (2014).
- Minami, T., Nishi, Y. & Miyata, T. Impact of incorporating sodium into polycrystalline p-type Cu₂O for heterojunction solar cell applications. *Appl. Phys. Lett.* **105**, 1–6 (2014).
- Brochen, S. *et al.* Effect of strontium incorporation on the p-type conductivity of Cu₂O thin films deposited by metal–organic chemical vapor deposition. *J. Phys. Chem. C* **acc.jpcc.6b05479** (2016). <https://doi.org/10.1021/acs.jpcc.6b05479>.
- Kardarian, K. *et al.* Effect of Mg doping on Cu₂O thin films and their behavior on the TiO₂/Cu₂O heterojunction solar cells. *Sol. Energy Mater. Sol. Cells* **147**, 27–36 (2016).
- Kumar, S. S., Kulandaisamy, J. I., Arulanantham, S. V. A. M. S. & Alfaify, V. G. S. Enhanced optoelectronic properties of Mg doped: Cu₂O thin films prepared by nebulizer pyrolysis technique. *J. Mater. Sci. Mater. Electron.* <https://doi.org/10.1007/s10854-019-01397-8> (2019).
- Resende, J., Jiménez, C., Nguyen, N. D. & Deschanvres, J. L. Magnesium-doped cuprous oxide (Mg:Cu₂O) thin films as a transparent p-type semiconductor. *Phys. Status Solidi Appl. Mater. Sci.* **213**, 2296–2302 (2016).
- Resende, J. *et al.* Resilience of cuprous oxide under oxidizing thermal treatments via magnesium doping. *J. Phys. Chem. C* **123**, 8663–8670 (2019).
- Vandervorst, W. *et al.* Dopant, composition and carrier profiling for 3D structures. *Mater. Sci. Semicond. Process.* **62**, 31–48 (2017).
- Amouyal, Y. & Schmitz, G. Atom probe tomography—A cornerstone in materials characterization. *MRS Bull.* **41**, 13–18 (2016).
- Larson, D. J., Prosa, T. J., Perea, D. E., Inoue, K. & Mangelinck, D. Atom probe tomography of nanoscale electronic materials. *MRS Bull.* **41**, 30–34 (2016).
- Zhou, X., Yu, X. X., Kaub, T., Martens, R. L. & Thompson, G. B. Grain boundary specific segregation in nanocrystalline Fe(Cr). *Sci. Rep.* **6**, 1–14 (2016).
- Stokes, A., Al-Jassim, M., Diercks, D., Clarke, A. & Gorman, B. Impact of wide-ranging nanoscale chemistry on band structure at Cu(In, Ga)Se₂ grain boundaries. *Sci. Rep.* **7**, 1–11 (2017).
- König, D. *et al.* Location and electronic nature of phosphorus in the Si nanocrystal: SiO₂ system. *Sci. Rep.* **5**, 1–10 (2015).
- Gault, B. *et al.* Estimation of the reconstruction parameters for atom probe tomography. *Microsc. Microanal.* **14**, 296–305 (2008).
- Gault, B. *et al.* Ultramicroscopy Advances in the reconstruction of atom probe tomography data. *Ultramicroscopy* **111**, 448–457 (2011).
- Vurpillot, F. *et al.* Advanced volume reconstruction and data mining methods in atom probe tomography. 46–52 (2016). <https://doi.org/10.1557/mrs.2015.312>.

27. Gault, B. *et al.* Behavior of molecules and molecular ions near a field emitter. *New J. Phys.* **18**, 1 (2016).
28. Stepień, Z. M. & Tsong, T. T. Formation of metal hydride ions in low-temperature field evaporation. *Surf. Sci.* **409**, 57–68 (1998).
29. Deuermeier, J. *et al.* Visualization of nanocrystalline CuO in the grain boundaries of Cu₂O thin films and effect on band bending and film resistivity. *APL Mater.* **6**, (2018).
30. Wei, Y. *et al.* 3D nanostructural characterisation of grain boundaries in atom probe data utilising machine learning methods. *PLoS ONE* <https://doi.org/10.1371/journal.pone.0225041> (2019).
31. Miller, M. K. & Hetherington, M. G. Local magnification effects in the atom probe. *Surf. Sci.* [https://doi.org/10.1016/0039-6028\(91\)90449-3](https://doi.org/10.1016/0039-6028(91)90449-3) (1991).
32. Vayyala, A. *et al.* A nanoscale study of thermally grown chromia on high-Cr ferritic steels and associated oxidation mechanisms. *J. Electrochem. Soc.* <https://doi.org/10.1149/1945-7111/ab7d2e> (2020).
33. Mancini, L. *et al.* Composition of wide bandgap semiconductor materials and nanostructures measured by atom probe tomography and its dependence on the surface electric field. *J. Phys. Chem. C* **118**, 24136–24151 (2014).
34. Han, S. & Flewitt, A. J. Analysis of the conduction mechanism and copper vacancy density in p-type Cu₂O thin films. 1–8 (2017) [doi:https://doi.org/10.1038/s41598-017-05893-x](https://doi.org/10.1038/s41598-017-05893-x).
35. Han, S. & Flewitt, A. J. Control of grain orientation and its impact on carrier mobility in reactively sputtered Cu₂O thin films. *Thin Solid Films* **704**, 138000 (2020).
36. Yildiz, A., Serin, N., Serin, T. & Kasap, M. The effect of intrinsic defects on the hole transport in Cu₂O. *Optoelectron. Adv.* **3**, 1034–1037 (2016).
37. Tapiero, M., Zielinger, J. P. & Noguét, C. Electrical conductivity and thermal activation energies in Cu₂O single crystals. *Phys. Status Solidi* **12**, 517–520 (1972).
38. Hodby, J. W., Jenkins, T. E., Schwab, C., Tamura, H. & Trivich, D. Cyclotron resonance of electrons and of holes in cuprous oxide, Cu₂O. *J. Phys. C Solid State Phys.* **9**, 1429–1439 (1976).
39. Nolan, M. & Elliott, S. D. Tuning the transparency of Cu₂O with substitutional cation doping. *Chem. Mater.* **20**, 5522–5531 (2008).
40. Figueiredo, V. *et al.* p-Type CuO thin-film transistors produced by thermal oxidation. *J. Disp. Technol.* **9**, 735–740 (2013).
41. Nolan, M. & Elliott, S. D. The p-type conduction mechanism in Cu₂O: A first principles study. *Phys. Chem. Chem. Phys.* **8**, 5350–5358 (2006).
42. Isseroff, L. Y. & Carter, E. A. Electronic structure of pure and doped cuprous oxide with copper vacancies: Suppression of trap states. *Chem. Mater.* **25**, 253–265 (2013).
43. Wang, Y. *et al.* Controlling the preferred orientation in sputter-deposited Cu₂O thin films: Influence of the initial growth stage and homoepitaxial growth mechanism. *Acta Mater.* **76**, 207–212 (2014).
44. Nguyen, V. H. *et al.* Electron tunneling through grain boundaries in transparent conductive oxides and implications for electrical conductivity: The case of ZnO:Al thin films. *Mater. Horizons* <https://doi.org/10.1039/c8mh00402a> (2018).
45. Ishizuka, S., Kato, S., Okamoto, Y. & Akimoto, K. Control of hole carrier density of polycrystalline Cu₂O thin films by Si doping. *Appl. Phys. Lett.* **80**, 950–952 (2002).
46. Minami, T., Nishi, Y. & Miyata, T. Heterojunction solar cell with 6% efficiency based on an n-type aluminum-gallium-oxide thin film and p-type sodium-doped Cu₂O sheet. *Appl. Phys. Express* **8**, 022301 (2015).
47. Murali, D. S. *et al.* Synthesis of Cu₂O from CuO thin films: Optical and electrical properties. *AIP Adv.* **5**, 047143 (2015).
48. Ye, F. *et al.* Doping cuprous oxide with fluorine and its band gap narrowing. *J. Alloys Compd.* **721**, 64–69 (2017).
49. Biccari, F., Malerba, C. & Mittiga, A. Chlorine doping of Cu₂O. *Sol. Energy Mater. Sol. Cells* **94**, 1947–1952 (2010).
50. Ye, F. *et al.* The electrical and thermoelectric properties of Zn-doped cuprous oxide. *Thin Solid Films* **603**, 395–399 (2016).
51. Kikuchi, N., Tonoooka, K. & Kusano, E. Mechanisms of carrier generation and transport in Ni-doped Cu₂O. *Vacuum* **80**, 756–760 (2006).
52. Prabhu, R. D., Herisalin, S. V. H. A., Jegatha, G. A. & Jeyadheepan, C. K. Effect of Neodymium doping on the structural, morphological, optical and electrical properties of copper oxide thin films. *J. Mater. Sci. Mater. Electron.* **29**, 10921–10932 (2018).
53. Thompson, K. *et al.* *In situ site-specific specimen preparation for atom probe tomography.* **107**, 131–139 (2007).
54. Miller, M. K. & Russell, K. F. *Atom probe specimen preparation with a dual beam SEM / FIB miller.* **107**, 761–766 (2008).

Acknowledgements

Financial support by the IDS-FunMat scholarship selected under the program “ERASMUS MUNDUS II 2009–2013” is gratefully acknowledged. N. D. N. acknowledges the financial support by the F.R.S-FNRS of Belgium (project J.0124.19) and by the European Joint Doctorate FUNMAT (H2020-MSCA-ITN-2014, Project ID 641640). This project was financially supported by “Carnot Energies du Futur” (SOLAROX project). This work benefited from the facilities and expertise of the OPE(N)RA characterization platform of FMNT (FR 2542, fmnt.fr) supported by CNRS, Grenoble INP and UGA. The authors would like to thank to Laetitia Rapenne for the TEM analysis.

Author contributions

J.R., C.J., J.-L.D. and N.D.N. designed the experiments. J.R. conducted the material synthesis and structural characterization. V.-S.N. was responsible for the temperature dependent Hall Effect measurements and in collaboration with S.B. and W.F. developed the two acceptor levels model. C.F. was responsible to conduct the atom probe tomography and in collaboration with W.V. treated and interpreted the data. L.B. contributed to the scientific discussion on the dopants of copper oxide. C.J., J.-L.D. and N.D.N. provided the support in the results discussion. J.R. wrote the main manuscript text and prepared the images. All authors provided feedback and edits.

Competing interests

The authors declare no competing interests.

Additional information

Supplementary Information The online version contains supplementary material available at <https://doi.org/10.1038/s41598-021-86969-7>.

Correspondence and requests for materials should be addressed to J.R.

Reprints and permissions information is available at www.nature.com/reprints.

Publisher's note Springer Nature remains neutral with regard to jurisdictional claims in published maps and institutional affiliations.



Open Access This article is licensed under a Creative Commons Attribution 4.0 International License, which permits use, sharing, adaptation, distribution and reproduction in any medium or format, as long as you give appropriate credit to the original author(s) and the source, provide a link to the Creative Commons licence, and indicate if changes were made. The images or other third party material in this article are included in the article's Creative Commons licence, unless indicated otherwise in a credit line to the material. If material is not included in the article's Creative Commons licence and your intended use is not permitted by statutory regulation or exceeds the permitted use, you will need to obtain permission directly from the copyright holder. To view a copy of this licence, visit <http://creativecommons.org/licenses/by/4.0/>.

© The Author(s) 2021